Available online at www.sciencedirect.com
ScienceDirect
Journal of Hazardous Materials 140 (2007) 478–487
Journal of Hazardous Materials
www.elsevier.com/locate/jhazmat

Coupling dynamic blow down and pool evaporation model for LNG

John L. Woodward *

Baker Engineering and Risk Consultants, Inc., 3330 Oakwell Court, Suite 100, San Antonio, TX 78218-3024, United States

Available online 21 October 2006

Abstract

Treating the dynamic effects of accidental discharges of liquefied natural gas (LNG) is important for realistic predictions of pool radius. Two phenomena have important influence on pool spread dynamics, time-varying discharge (blow down) and pool ignition. Time-varying discharge occurs because a punctured LNG tanker or storage tank drains with a decreasing liquid head and decreasing head-space pressure. Pool ignition increases the evaporation rate of a pool and consequently decreases the ultimate pool area. This paper describes an approach to treat these phenomena in a dynamic pool evaporation model.

The pool evaporation model developed here has two separate regimes. Early in the spill, momentum forces dominate and the pool spreads independently of pool evaporation rate and the corresponding heat transfer rate. After the average pool depth drops below a minimum value, momentum forces are largely dissipated and the thin edges of the pool completely evaporate, so pool area is established by the heat transfer rate. The maximum extent of a burning pool is predicted to be significantly less than that of an unignited pool because the duration of the first regime is reduced by higher heat transfer rates. The maximum extent of an LNG pool is predicted to be larger upon accounting for blow down compared with using a constant average discharge rate. However, the maximum pool extent occurs only momentarily before retreating.

Keywords: Time-varying discharge; Cryogenic liquid spills; LNG evaporation; LNG pool fire; Pool spread and evaporation

1. Introduction

The hazards of importing liquefied natural gas (LNG) have been the subject of a considerable body of literature [1–5]. The focus of hazard analysis has been primarily on large-scale pool fires. Flash fire hazards are of secondary importance because of the brevity of exposure at a given location. Explosion hazards are generally considered unlikely in marine operations because of the absence of congested structure to accelerate flame speeds. Explosion hazards to LNG vaporization terminals are considered a localized threat, of primary significance to the terminal facilities, although close neighbors could be affected.

In this paper we develop predictions that account for the dynamics of LNG pool spread and evaporation. This extends earlier work on the development of discharge, rainout, and pool evaporation models [6–8] including the most recent SafeSite$_{3G}$^{TM} model [9,10]. By accounting for the dynamics of pool discharge and pool spread, the entire event takes on more characteristics of a flash fire. The physical phenomena that influence the extent of LNG pools and fires, are time dependent discharge rates, time dependent pool spread and the effect of ignition on pool evaporation rate. These are discussed in turn.

2. Discharge duration decreases inversely with discharge rate

Two types of LNG carriers are in common use, the membrane type and the Moss sphere type. Both are of double hull construction. A membrane carrier has typically five LNG tanks with a cross-section illustrated in Fig. 1. Individual membrane tanks are usually larger than an individual Moss sphere, and lay lower in the water than Moss spheres.

Time-dependent discharge or blow down develops when an LNG tank is punctured below the LNG liquid level. The driving force for liquid discharge is the head pressure plus the liquid head, both of which decrease in time. The head pressure decreases because of the piston effect that enlarges the vapor space. Internal evaporation increases the vapor in the headspace, but usually not fast enough to avoid developing a slight vacuum in atmospheric tanks. A vacuum breaker valve

* Tel.: +1 210 824 5960.
E-mail address: woodward@wbeng.com.

0304-3894/$ – see front matter © 2006 Elsevier B.V. All rights reserved.
doi:10.1016/j.jhazmat.2006.10.050

Nomenclature

A_h	effective cross-sectional area of puncture (m^2)
A_{pool}	pool area (m^2)
A_T	cross-sectional area of tank (m^2)
b	burning regression rate (m/s)
C_D	discharge coefficient, dimensionless
e_v	error between vapor densities ρ_g and ρ_V (kg/m^3)
E_L	mass of liquid emitted from tank (kg)
F_{dis}	discharge rate (kg/s)
F_D	viscous drag force (N)
F_{evap}	evaporation rate (kg/s)
F_g	gravity spreading force (N)
F_I	inertial spreading force (N)
F_S	surface tension force (N)
g	gravitational constant (m/s^2)
G_{dis}	discharge flux ($kg/(m^2\ s)$)
G_{evap}	evaporation flux ($kg/(m^2\ s)$)
h	height of liquid layer (partly submerged) (m)
ΔH	change in specific enthalpy (J/kg)
I_V	internal evaporation rate in tank (kg/s)
m_{air}	mass of air in tank vapor (kg)
m_L	mass of liquid in tank (kg)
m_V	mass of vapor in tank (kg)
M_i	mole weight of component i (kg/kg mol)
M_V	molecular weight of vapor (kg/kg mol)
$M_{w\ air}$	molecular weight of humid air (kg/kg mol)
P_{amb}	ambient or back pressure (Pa(a))
P_{hole}	pressure at mid-point of rupture, including hydraulic head (Pa(a))
P_T	head pressure in tank (Pa(a))
P_{vap}	vapor pressure (Pa)
$\Delta P_{v\ set}$	set point for vacuum breaker valve (Pa(g))
R	gas constant (J/(kg mol K))
R_{pool}	radius of pool (m)
t	time (s)
T_T	temperature of tank contents (K)
u	velocity of discharging fluid (m/s)
v_V	specific volume of vapor (m^3/kg)
V_V	volume of vapor space in tank (m^3)
w_{air}	mass fraction of air in vapor
y_{air}	mole fraction of air in vapor
y_I	mole fraction of inerts in vapor (inerts could be initial air in tank)
z_L	non-frothy liquid level in tank (m)
z_T	interior height of tank (m)

Greek letters

μ_w	viscosity of water (Pa s)
$\Delta\rho$	normalized buoyancy
ρ_g	vapor density calculated from equation of state (kg/m^3)
ρ_L	liquid density (kg/m^3)
ρ_V	vapor density calculated as mass/volume (kg/m^3)
ρ_w	density of water (kg/m^3)
σ	net surface tension on spreading liquid (N/m)

Subscript

k	Current time increment

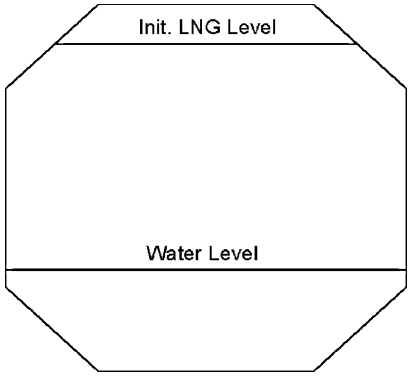

Fig. 1. Typical cross-section of membrane tank LNG carrier.

may open intermittently during the blow down and restore the head pressure to atmospheric, causing slight increases in discharge rate. In the example case below, with a 3 m equivalent diameter puncture, the vacuum breaker valve is predicted to open essentially every 20 s. The pertinent equations solved for a blow down model are detailed in Appendix A.

As an example case, consider a double-hull membrane type LNG carrier with five tanks averaging 35,000 m^3 of LNG each. Typically, 25,000 m^3 is above the water level giving a liquid level of about 17 m above the water level. A puncture of both the inner and out hull is postulated at the water level. The composition of LNG varies primarily with the source location of the LNG, and ranges typically from 80% to about 97% methane. We use here a hypothetical middle-range composition listed in Table 1.

Blow down predictions are shown for various postulated equivalent diameter of punctures to the inner and outer hull in Figs. 2 and 3. Fig. 2 plots liquid level on a logarithmic time scale. With large equivalent diameter hole sizes of 3 and 5 m the level drops quickly and the discharge duration is short. The predicted discharge rate is shown in Fig. 3, decaying in time. The discharge rate curves tail off, and this tail has been omitted in Fig. 3. The drain time listed in Table 2 is taken to the point where discharge rate tails off (the last point in Fig. 3).

The effect of tank shape is seen in Figs. 4 and 5. Fig. 4 plots the tank volume for a membrane tank with the proportions shown

Table 1
LNG composition modeled

Component	Mole (%)	Mass (%)
Methane	91.0	83.13
Ethane	7.921	13.56
Propane	0.372	0.934
iso-Butane	0.521	1.725
n-Butane	0.149	0.493
iso-Pentane	0.037	0.152
Total	100.000	100.000

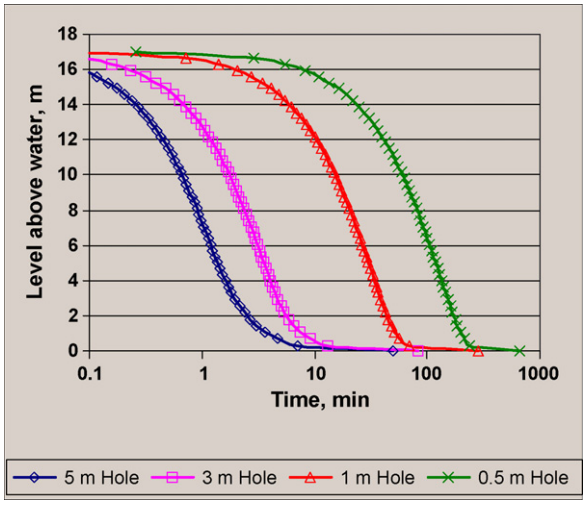

Fig. 2. Tank level with various equivalent hole diameter for blow down of LNG carrier.

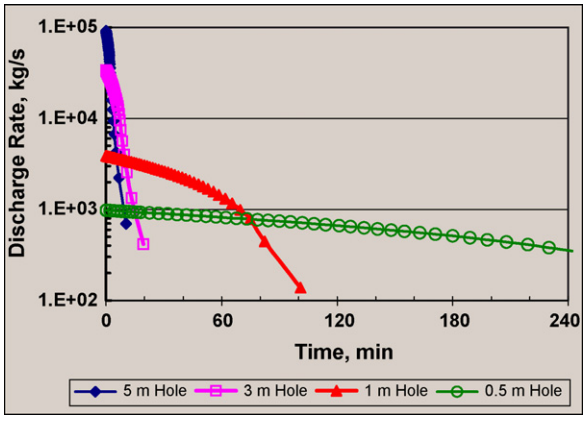

Fig. 3. Discharge rates for blow down of LNG carrier.

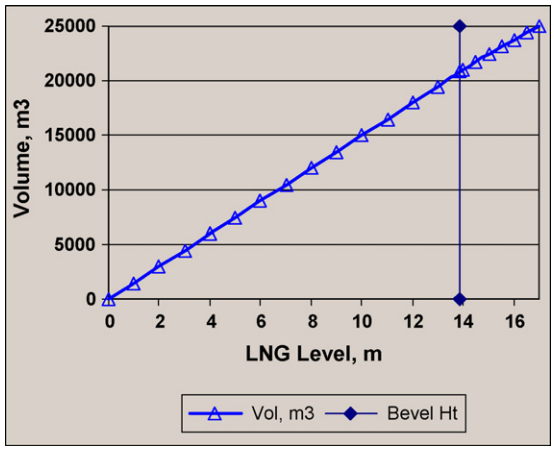

Fig. 4. Tank volume vs. LNG level for beveled membrane tank.

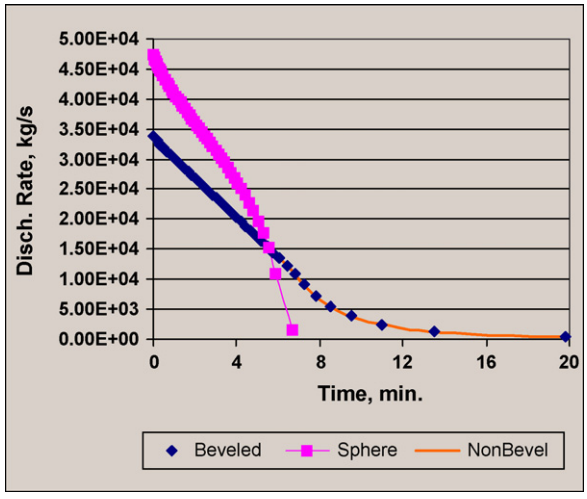

Fig. 5. Effect of tank geometry on discharge rate for 3 m hole.

in Fig. 1. With these proportions the initial LNG level is 3.24 m above the lower corner of the bevel and 17 m above the water level. The bevel is 6.6 m on each side, and the tank height and width are 28 and 30 m, respectively. The effect of the bevelled tank cross-section is minor.

Fig. 5 plots the blow down discharge rate for a bevelled membrane tank, a rectangular membrane tank, and a spherical tank of volume 25,000 m^3 to be comparable with the membrane tank example cases. Normally, Moss spheres are smaller than membrane tanks. Clearly, the response of the bevelled tank is very nearly identical with that of a rectangular tank. The spherical tank begins with a larger liquid head and a corresponding higher initial discharge rate, and consequently has a shorter drain time. The shape of the discharge curve for a spherical tank is slightly different from that for the membrane tank as well.

Table 2
Summary of predicted blow down duration for LNG carriers

Hole diameter (m)	Initial discharge rate (kg/s)	Average discharge rate (kg/s)	Drain time (min)
0.5	980	522	354
1	3,890	1,834	101
3	33,930	9,490	19.7
5	91,200	19,600	9.43

3. Spreading LNG pool with constant discharge rate

For a constant discharge rate of LNG onto water, a steady state pool area is developed in a reasonably short time. At steady state, the discharge rate, F_{dis}, equals the evaporate rate, F_{evap}, at a pool area, A_{pool}. For cryogenic liquids, including LNG, evaporating on water, the evaporation rate flux, G_{evap} defined as F_{evap}/A_{pool} is constant, so at steady state:

$$F_{evap} = F_{dis} \tag{1}$$

$$A_{pool}(t) = \frac{F_{dis}(t)}{G_{evap}} \tag{2}$$

for a circular pool, pool radius, R_{pool}, is:

$$R_{pool} = \left(\frac{A_{pool}}{\pi}\right)^{1/2} \tag{3}$$

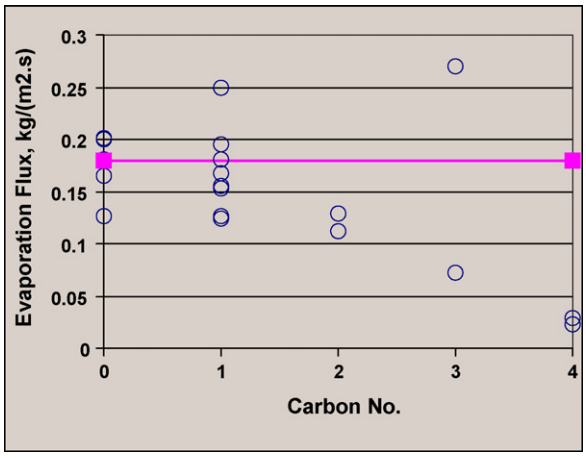

Fig. 6. Measured evaporation flux for cryogenic liquids on water.

There is speculation that the evaporation flux is not actually constant but depends upon the degree of turbulence generated during the spill. If the spill drops from a height and penetrates the water level, increased mixing and turbulence is likely, as evidenced by such experiments involving cryogenic liquids that resulted in a rapid phase transition explosion. According to this theory, the evaporative flux would be higher near the spill and decrease farther away. In the absence of experimental data, though, the assumption of a constant evaporation flux cannot be improved upon at present.

LNG evaporation rate experiments have been summarized, including reviews by ABS [1] and Prince [2]. Experimental data on the evaporation flux of cryogenic liquids on water are summarized in Fig. 6 from various sources cited by Prince and listed in Table 3. There is likely a composition effect on the LNG test data, but no attempt is made to adjust the carbon number to accommodate this fact. From Fig. 6, an average rate for the evaporation flux of LNG (as methane) on water is 0.180 kg/(m^2 s).

Table 3
Evaporation rate data for cryogenic liquids on water

Spilled liquid	G_{evap} (kg/(m^2 s))	Reference
Nitrogen	0.127, 0.201	[14]
Nitrogen	0.165	[15]
Methane	Max. 0.180	[16]
Methane	0.180	[17]
LNG	0.181	[14]
LNG	0.155	[15]
LNG	0.181	[18]
LNG	0.200	[19]
LNG	0.195	[20]
LNG	0.195	[21]
LNG	0.156	[22]
LNG	0.124, 0.126, 0.153	[23]
LNG	0.250	[24]
LNG	0.168	[25]
Ethylene	0.129	[18]
Ethane	0.112	[18]
Propane	0.0718	[18]
	0.270	[24]
n-Butane	0.0234, 0.0293	[24]
n-Butane	0.0290	[18,26]

Table 4
Burning and evaporation flux for LNG on water from China Lake Tests [13]

Experiment	Burning G_{evap} (kg/(m^2 s))
3	0.431
5	0.401
6	0.361
12	0.221
1	0.199
7	0.154
4	0.152

For comparison, the evaporation flux for LNG on insulating concrete was found in the Montoir 35 m diameter tests [11] to be 0.14 kg/(m^2 s). By minimizing the contribution of heat conduction from the substrate, this represents the isolated contribution of heat from the fire. However, as discussed by Raj [4] it is lower by about a factor of 2.5 from the value calculated using measurements on heat flux from the fire.

Only a few experiments have been conducted of burning LNG on water. Mizner and Eyre [12] spilled LNG at Maplin Sands in the UK and measured fire radiation but did not measure the evaporation rate. Experiments at China Lake, CA reported by Raj et al. [13] found values listed in Table 4.

Various authors have postulated a value for the ratio of burning to non-burning evaporation flux of LNG on water, as shown in Table 5. Taking the non-burning evaporation flux as 0.180 kg/(m^2 s), the postulated values for burning evaporation flux are also listed in Table 5. The regression rate, b, is related to the evaporation flux by

$$b = \frac{G_{evap}}{\rho_L} \tag{4}$$

Using a value for the liquid density of 449 kg/m^3 gives the burning regression rate in Table 5. The non-burning regression rate corresponding to 0.18 kg/m^2 s is 0.40 mm/s. For comparison, the burning regression rate for fresh gasoline and diesel varies from 0.03 to 0.1 mm/s according to Ref. [27] cited by Ref. [28].

Values of the burning to non-burning flux ratio should be greater than unity. We use here the value of 0.45 kg/(m^2 s) for the evaporation rate of LNG burning on water (a factor of 2.5 times the unignited rate).

The SafeSite$_{3G}$^{TM} model [9,10] is used to predict LNG pool radius for an unconstrained spreading pool on water (no influence of the LNG carrier) using a constant average discharge rate and the discharge duration as the drain time, both from Table 2.

Table 5
Ratio of evaporation flux on water for burning to non-burning LNG

Ratio	Burning G_{evap} (kg/(m^2 s))	Burning regression rate (mm/s)	Reference
2.5	0.450	1.0	[29,30]
1.89	0.340	0.757	[31]
1.41	0.254	0.567	[5]
0.62	0.112	0.249	[28]
0.40	0.072	0.160	[32]

Table 6
Steady-state pool radius for unignited and burning pool

Hole diameter (m)	Average discharge rate (kg/s)	Unignited pool radius (m)	Time to reach steady state (s)	Burning pool radius (m)	Time to reach steady state (min)
0.5	522	30.4	58	19.2	0.5
1	1,834	56.9	164	36.0	1.7
3	9,375	129	316	81.4	2.0
5	19,610	186	345	118	3.7

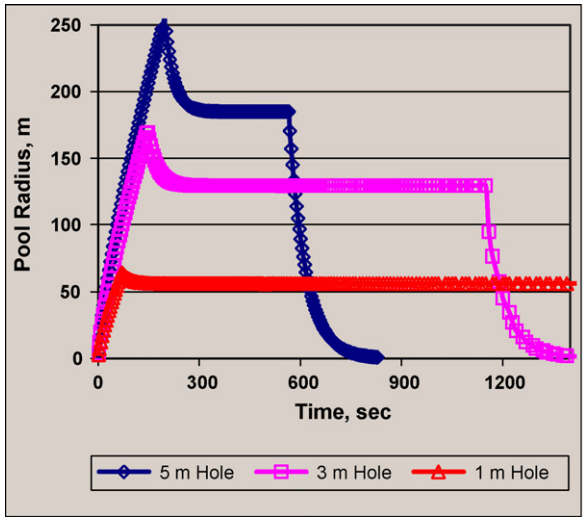

Fig. 7. Pool radius for spreading unignited LNG on water using constant average discharge rate.

The pool spread model predicts a pool radius that slightly overshoots the steady-state pool size as shown in Fig. 7. The predicted steady-state pool size agrees with expectations in Table 6. The duration at which the pool is predicted to be at steady state becomes shorter with larger equivalent hole diameters. Quiao et al. [33] plot the steady-state pool radius against hole size and show that this curve saturates above hole sizes of about 5 m, approaching the size for an instantaneous spill. The predicted pool evaporation rate equals the liquid discharge rate at steady state as illustrated in Fig. 8 for a 3 m hole.

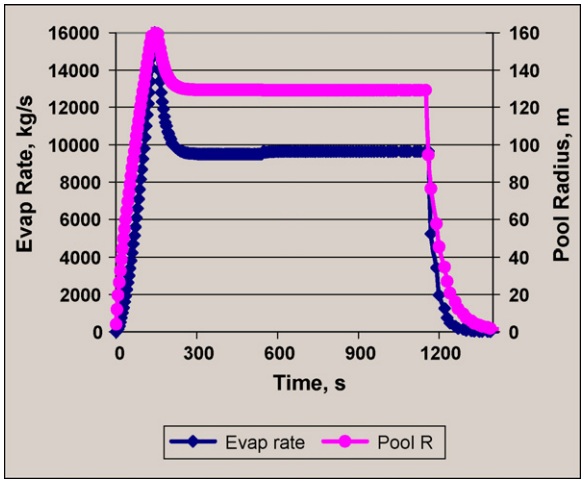

Fig. 8. LNG unignited pool evaporation rate and pool radius for 3 m hole.

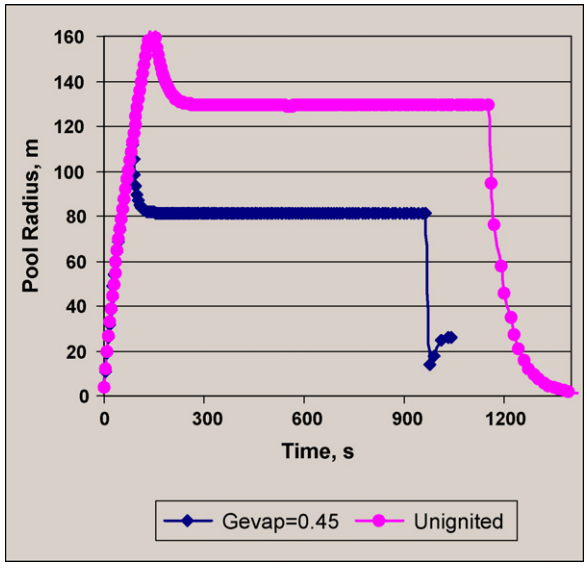

Fig. 9. Comparison of ignited and unignited LNG pool for constant average discharge rate from 3 m hole.

4. Effect of ignition on LNG pool size for constant discharge rate

Clearly, an ignited LNG pool on water will reach a much smaller steady-state pool. Fig. 9 plots the pool radius for an unignited and a burning pool for a constant discharge rate from a 3 m diameter hole. If ignition occurs at any time, the pool radius would be expected to move over some time from the upper curve to the lower.

5. Spreading LNG pool coupled with dynamic discharge rate for unignited pool

The blow down discharge rates are used as the input rate to the pool spread and evaporation model (PEV) in the SafeSite$_{3G}$^{TM} model. This assumes that the 5 m spill behaves more like a continuous than an instantaneous release. The PEV model makes use of the analytic solution of Dodge et al. [34] for continuous releases given in Appendix B. Dodge et al., similar to Fay [31,35] identify three spreading regimes. The first is the "gravity-inertia" regime where the gravity spreading and inertial forces are approximately equal. This is followed by the "gravity-viscous" regime where the gravity spreading and viscous drag forces are approximately equal. For non-volatile materials that may spread to form thin slicks the third regime may occur, the

"viscous-surface tension" regime where the viscous drag and surface tension forces are dominant.

Alternative assumptions can be applied for the actual pool depth gradients across the pool. The simplest assumptions are

(1) The pool depth is thickest at the source and thinnest at the leading edge. This is likely to be the case for a continuous discharge.
(2) The pool depth is thickest at the leading edge. This has been observed for experiments in which the spill is nearly instantaneous. The spilled mass is largely contained in the spreading interface, leaving a thin layer behind.

In the first assumption, the pool radius will retreat by evaporation of the thin leading edge. In the second assumption, the pool will evaporate first in an inner core, so a trailing edge of the pool develops and moves forward until it catches up with the leading edge as the last bit of LNG evaporates. That is, applying a linear gradient with the first assumption, the average pool height, h, is at mid-radius, and the gradient is given by

$$\frac{\Delta h}{\Delta R} = \frac{2h}{R} \tag{5}$$

Idealizing the linear gradient to zero height, by the definition of regression rate, b, the mass in the leading edge between a height of $2b$ and zero will completely evaporate in 1 s. So when the average pool height reaches $h_{\min}$, taken as 10 mm, the pool will retreat a radial increment of ΔR given by

$$\Delta R = 2b\frac{\Delta R}{\Delta h} = 2b\frac{R}{h_{\min}} = \frac{0.8}{10}R \text{ (non-burning pool)} \tag{6}$$

In practice, the PEV module numerically solves standard mass and energy balance differential equations listed in Appendix A. An average pool depth, h, is found as the time-varying mass of liquid in the pool, m_{pool}, divided by the area of the liquid pool, A_{pool}. When the pool depth drops below a minimum average value, $h_{\min}$, then the next pool area is set to the steady-state value given by Eq. (2). This keeps the average pool depth equal to the minimum depth and effectively accomplishes the radius reduction given by Eq. (6).

With this approach the predictions for pool radius are as shown in Figs. 10 and 11. The steady-state pool radius calculated using Eqs. (2) and (3) with a current value for the discharge rate is shown along with the pool radius predicted by the PEV model. The solution for a 1 m hole, the light solid line in Fig. 10, slightly overshoots the steady-state solution and then is set equal to the steady-state value when the average depth reaches the $h_{\min}$ value. For a 3 m hole, the solution is similar, but with a more pronounced overshoot of the steady-state solution.

In Fig. 11, the PEV solution for a 5 m hole (open diamonds) peaks at a radius of 240 m, a lower maximum pool radius than that for a 3 m hole. The solution for a 3 m hole (open circles) reaches a peak value of 294 m before decaying to the follow the steady-state pool radius. The reason for this difference is explained by the properties of the time-varying discharge rate solution.

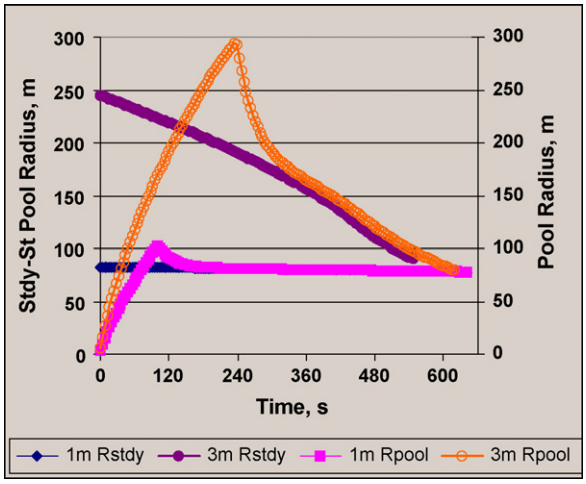

Fig. 10. Pool radius with time-varying source rate from blow down and an unignited LNG pool with a thin leading edge for a 1 and 3 m hole, 25,000 m^3.

First, the peak radius values for a time-varying discharge rate solution (Figs. 10 and 11) are higher than those for a constant discharge rate (Fig. 7) because the time varying discharge rates are higher than the average discharge rate early in the response. Consequently, the early high discharge rates from large holes produce a high-momentum pool spread until either the blow down rate slows dramatically or the average pool depth reaches a minimum at which a thinning pool shrinks.

To illustrate the first point, the blow down rate for a 5 m hole slows perceptibly just past 120 s. This time is at the knee of the blow down curve in Fig. 2. Fig. 2 is expanded and put on a linear scale in Fig. 12 to make this clear. The knee of the blow down curve for a 3 m hole occurs later, at about 350 s, and by that time the pool has reached its minimum pool thickness and is retreating.

Secondly, the PEV solutions begin to decline after the average pool depth is depleted to the minimum value. This is made clear by plotting the predicted average pool depth versus time in Fig. 13. Pool depletion forces a reduction in pool area after about 240 s for a 3 m hole, and after about 120 s for a 5 m hole.

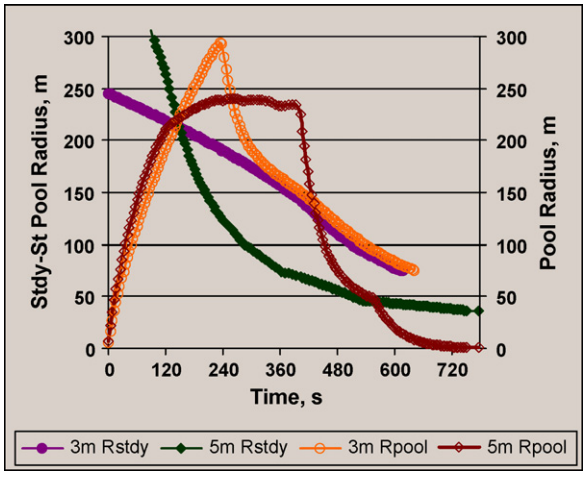

Fig. 11. Pool radius with time-varying source rate from blow down and an unignited LNG pool with a thin leading edge for a 3 and 5 m hole.

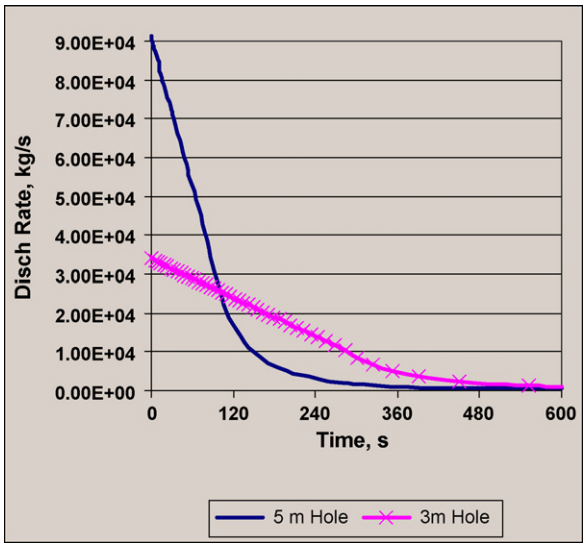

Fig. 12. Early portion of blow down curve for 3 and 5 m holes.

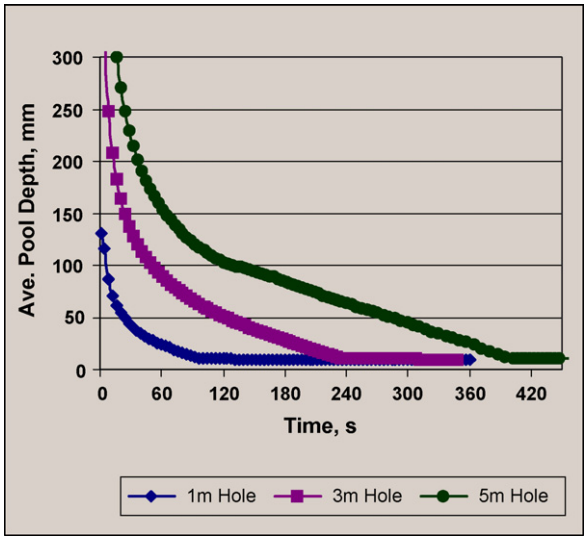

Fig. 13. Average pool depth as predicted by the PEV model for 1, 3 and 5 m holes.

6. Effect of ignition on pool with time-varying discharge rate

As would be expected, the maximum pool radius is reduced when the pool is ignited. Figs. 14 and 15 compare the unignited and the ignited pool predictions for holes of 1, 3, and 5 m equivalent diameter. With the assumptions of the PEV model, the pool spread rate is initially independent of the evaporative flux rate, so the pool spread for a burning pool follows that of a non-burning pool. Since the burning evaporation rate is higher than a non-burning evaporation rate, the minimum pool thickness is reached sooner with a burning pool. At that point the pool contraction begins and the pool radius trends toward the limiting pool radius predicted by the steady-state formula, Eq. (2). With a burning pool, the maximum pool radius occurs with a 5 m hole, but this maximum is nearly the same as that for a 3 m hole.

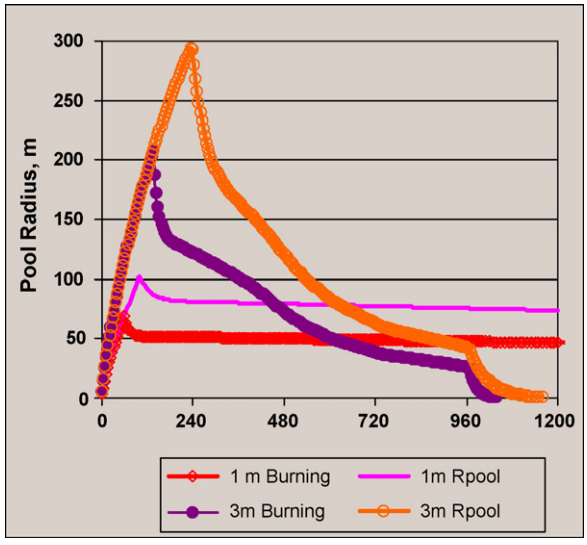

Fig. 14. Effect of igniting LNG pool on predicted pool radius for 1 and 3 m hole sizes.

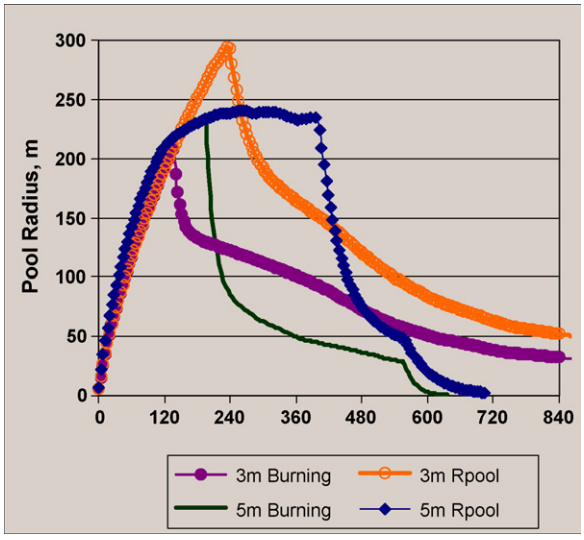

Fig. 15. Effect of igniting LNG pool on predicted pool radius for 3 and 5 m hole sizes.

7. Conclusions

The PEV pool evaporation model described here uses an analytic solution for pool spread as long as the average pool depth is above a minimum value. In this region, pool spread is insensitive to the heat transfer rate from the substrate to the pool, so both burning and non-burning pools are predicted to spread at the same rate. Upon applying a time-dependent discharge rate as the source rate to the pool, the early discharge rates force the pool radius to larger values than would be predicted using a constant average discharge rate. The resulting large pool area produces an evaporation rate higher than the source rate, so the pool inventory depletes and the average pool depth decreases. When the average pool depth drops below a minimum value, taken here as 10 mm, the depth is held constant and pool area is calculated from the pool inventory as the volume to depth ratio.

The evaporation rate is calculated from the constant evaporative flux rate times pool area. With this approach, the predicted pool area decreases. By assuming that the leading edge is thinner than the depth at the source, the leading edge recedes. The pool radius for a burning pool is smaller than that for a non-burning pool while the pool is shrinking.

For a non-burning pool, the PEV model with a time-varying discharge rate predicts that a maximum pool radius will occur with about a 3 m diameter hole. The predicted pool radius using a time-varying source rate is larger, at early response times, than that predicted using a constant average discharge rate. However, the maximum pool radius occurs only momentarily. In contrast, there is a larger duration to the steady-state pool radius that develops if a constant discharge rate is assumed. The duration of the steady-state period for a constant discharge rate decreases with increasing hole size.

Upon ignition, the LNG pool area is predicted to decrease if the pool has already expanded to the point where the average pool depth has dropped below a minimum value, taken here as 10 mm. However, if ignition occurs before this point, pool spreading is unaffected by ignition, but rather is controlled by momentum terms.

Appendix A

A.1. Blow down modeling theory

There are two types of LNG carriers, Moss spheres and membrane carriers. As coded in the SafeSite$_{3D}$™ model, both types of geometry are treated. For spherical geometry the cross-sectional area is a function of liquid level, $A_T(z_L)$. For simplicity here, the geometry of a tank in a membrane carrier is described as a right rectangular volume of width, W_T, length, L_T, and height, z_T, so the cross-sectional area, A_T, is constant at $W_T L_T$. In code, the level is found from the liquid volume and the geometry of the tank via a subroutine.

The mass in the tank above the water level of liquid, m_L, and of vapor, m_v, is given in terms of the liquid and vapor density, ρ_L, ρ_v that are functions of the tank head pressure, P_T, and temperature, T_T, that is assumed homogeneous

$$m_L(t) = z_L(t) A_T \rho_L(T_T) \tag{A.1}$$

$$m_V(t) = (z_T - z_L(t)) A_T \rho_V(P_T, T_T) \tag{A.2}$$

and $z_L(t)$ is the height of the liquid. For a hole below the liquid level, the discharge rate, F_{dis}, defines the mass balance on the liquid above the water line. The discharge rate is defined in terms of the discharge coefficient, C_D, the cross-sectional area of the hole, A_h, and the discharge mass flux, G_{dis}, as:

$$\frac{dm_L}{dt} = F_{dis}(t) = C_D A_h G_{dis} \tag{A.3}$$

The vapor space mass balance can be similarly expressed by differentiating Eq. (A.2) with respect to time:

$$\frac{dm_V}{dt} = A_T \left[(z_T - z_L) \frac{\partial \rho_V}{\partial t} - \rho_V \frac{\partial z_L}{\partial t} \right] \tag{A.4}$$

In this form, the second term represents the piston effect of increasing the vapor space volume but requires some way to evaluate the derivative of vapor density. Fortunately, there is a way to find the vapor mass by focusing on vapor density and the internal evaporation rate. Vapor density can be calculated by two equally valid formulas. To distinguish these formulas, define ρ_g by the ideal gas equation of state, and ρ_v as the mass to volume ratio. Define time, t, as $k\Delta t$, and designate the current value of time-varying variables by the subscript k and the previous values by the subscript $k-1$:

$$\rho_{g,k} = \frac{M_{V,k} P_{T,k}}{R T_{T,k}} \tag{A.5}$$

$$\rho_{v,k} = \frac{m_{V,k}}{A_T (z_T - z_{L,k})} \tag{A.6}$$

The vapor space mass must increase in order to maintain the vapor density by an internal evaporation rate, I_v as the liquid level drops, or by air admitted by opening a vacuum breaker valve. Air admission is treated first in the calculating sequence, but for discussion, consider first the internal evaporation rate. A root-finding routine adjusts the internal evaporation rate, $I_{v,k}$, to drive the following function to within a specified tolerance of zero:

$$e_{v,k} = \frac{\rho_{v,k}}{\rho_{g,k}} - 1 \tag{A.7}$$

In the absence of air addition, the mass of vapor depends only on the previous mass plus the internal evaporation rate:

$$m_{V,k} = m_{V,k-1} + I_{v,k} \Delta t \tag{A.8}$$

The denominator in Eq. (A.7) remains relatively unchanged during the iterations to find the internal evaporation rate because the liquid temperature is insensitive to changes in internal evaporation rate and tank pressure and vapor molecular weight also vary slowly. However, the numerator in Eq. (A.7) is sensitive to $I_{v,k}$ so the convergence is generally rapid.

Air addition occurs when the vacuum breaker valve opens. Taking the set-point of the vacuum breaker valve as an increment $\Delta P_{v\,set}$ below atmospheric, P_{amb}, then the vapor space mass is given by:

$$m_{v,k} = m_{v,k-1} + I_{v,k} \Delta t \quad \text{if } P_T > P_{amb} - \Delta P_{v\,set} \tag{A.9a}$$

$$m_{v,k} = m_{v,k-1} + I_{v,k} \Delta t + \Delta m_{air} \quad \text{if } P_T \le P_{amb} - \Delta P_{v\,set} \tag{A.9b}$$

When the vacuum breaker valve opens, the incremental mass of air added, Δm_{air}, is added to bring the tank head pressure to atmospheric. The tank pressure is calculated from the vapor pressure at the liquid surface, $P_{vap}(T_{T,k-1})$ and the mole fraction of noncondensable components includes the added inerts, y_I, if any, plus air, y_{air}:

$$P_T = \frac{P_{vap}(T_T)}{1 - (y_I + y_{air})} \tag{A.10}$$

This equation is solved for the new mole fraction of air after setting the tank pressure to ambient pressure, or:

$$y_{\mathrm{air},k} = 1 - y_{\mathrm{I},k-1} - \frac{P_{\mathrm{vap}}(T_{\mathrm{T},k-1})}{P_{\mathrm{amb}}} \tag{A.11}$$

The molecular weight of the vapor mixture, M_{v}, is updated from the vapor components including air. The vapor density is updated using Eq. (A.5), and the mass increment of air, Δm_{air} is calculated from the mass fraction of air, $w_{\mathrm{air},k}$ found from the mole fraction of air:

$$M_{\mathrm{v},k} = \sum_{i=1}^{n} y_{i,k} M_i \tag{A.12}$$

$$w_{\mathrm{v\,air},k} = y_{\mathrm{v\,air},k} \frac{M_{\mathrm{w\,air}}}{M_{\mathrm{v},k}} \tag{A.13}$$

$$\Delta m_{\mathrm{air},k} = w_{\mathrm{v\,air},k} \rho_{\mathrm{v},k} V_{\mathrm{v},k} - m_{\mathrm{air},k-1} \tag{A.14}$$

Once the head space pressure is adjusted, the pressure at the mid-point elevation, z_{mid}, of the hole, P_{hole}, is found by adding the hydraulic head:

$$P_{\mathrm{hole},k} = P_{\mathrm{T},k} + g\rho_{\mathrm{L}}(z_{\mathrm{L},k-1} - z_{\mathrm{mid}}) \tag{A.15}$$

The discharge rate is found for a subcooled liquid discharge by the energy balance method for the velocity, u, in terms of the specific enthalpy of liquid, ΔH_{L}, which is found by integrating $v\,\mathrm{d}P$ with a constant specific volume, v_{Liq}:

$$\frac{1}{2}u^2 = -\Delta H_{\mathrm{L}} = -v_{\mathrm{Liq}}(t)[P_{\mathrm{hole}}(t) - P_{\mathrm{amb}}] \tag{A.16}$$

The mass flux is simply:

$$G_{\mathrm{dis}} = u\rho_{\mathrm{L}} \tag{A.17}$$

The liquid level is updated for the increment discharged, ΔF_{dis}, as well as the liquid mass evaporated. The inventory in the tank and emitted liquid, E_{L}, are updated

$$z_{\mathrm{L},k} = z_{\mathrm{L},k-1} - \frac{F_{\mathrm{dis},k}\Delta t - I_{\mathrm{v},k}\Delta t}{A_{\mathrm{T}}\rho_{\mathrm{L},k}} \tag{A.18}$$

$$m_{\mathrm{L},k} = m_{\mathrm{L},k-1} - F_{\mathrm{dis}}\Delta t - I_{\mathrm{v},k}\Delta t \tag{A.19}$$

$$E_{\mathrm{L},k} = E_{\mathrm{L},k-1} + F_{\mathrm{dis}}\Delta t \tag{A.20}$$

The time step size, Δt, is arbitrary for a subcooled liquid blow down. We typically use values that require about 500 steps for a complete blow down, and store the results for 50 of these steps to pass on to the pool spread and evaporation model. For stopping conditions, the blow down model can use a liquid level that is approaching the bottom elevation of the hole.

The blow down of a flashing liquid, or of the discharge from the vapor space of a flashing liquid is slightly more complicated, since it involves a frothy liquid that "swells" as the vapor bubbles lower the density. This case is also treated with the SafeSite$_{3G}$™ model.

Appendix B

B.1. Analytic solution for pool spread on water

The spread of liquids that dissolve, evaporate, and spread on water as given by Dodge et al. [34] equates the liquid spreading forces for different flow regimes in terms of the mass of liquid in the pool, m_{L}, the average pool depth, h, the density of spilled liquid, ρ_{L}, and water, ρ_{w}, the viscosity of the liquid, μ_{L}, water, μ_{w}, and air, μ_{a}, the pool radius, R, and time since the spill, t. The buoyancy term, $\Delta\rho$, is defined by:

$$\Delta\rho = 1 - \frac{\rho_{\mathrm{L}}}{\rho_{\mathrm{w}}} \tag{B.1}$$

The solution for a continuous release of rate $F_{\mathrm{dis}}(t)$ is the analytic solution of the differential equations formed by equating the terms first for the gravity spreading and inertial spreading forces and second for the gravity spreading and viscous flow forces to give:

- Gravity-inertia regime when $0 < t < t_3$

$$R(t) = 1.24\left(\frac{g\Delta\rho}{\rho_{\mathrm{L}}}\right)^{1/4} F_{\mathrm{dis}}(t)^{1/4} t^{3/4} \tag{B.2}$$

- Gravity-viscous regime when $t > t_3$

$$R(t) = 1.09\left[\frac{g\Delta\rho}{(\mu_{\mathrm{w}}/\rho_{\mathrm{w}})^{1/2}\rho_{\mathrm{L}}^2}\right]^{1/6} F_{\mathrm{dis}}(t)^{1/3} t^{7/12} \tag{B.3}$$

The transition between these regimes occurs at the time t_3 given by:

$$t_3 = \left(\frac{1.09}{1.24}\right)^6 \left(\frac{\rho_{\mathrm{w}}}{\rho_{\mathrm{L}} g\Delta\rho\mu_{\mathrm{w}}} F_{\mathrm{dis}}(t)\right)^{1/2} \tag{B.4}$$

A solution is given also for an instantaneous spill on water, in similar terms. Approximations are involved in applying these integral solutions with time-varying source rate and rapid evaporation since evaporation reduces the average liquid height, h, at each time step.

References

[1] ABS Consulting, "Consequence assessment methods for incidents involving releases from liquefied natural gas carriers", Report GEMS 1288209 for Federal Energy Regulatory Commission, Contract number FERC04C40196, May 13, 2004.
[2] M.L. Hightower, Gritzo, A. Luketa-Hamlin, J. Dovan, S. Tieszen, G. Wellman, M. Irwin, M. Kaneshige, B. Melof, C. Morrow, D. Ragland, Guidance on risk analysis and safety implications of a large liquefied natural gas (LNG) spill over water, Sandia National Laboratory Report, SAND2004-6258, U.S. Dept. of Energy, Washington, DC, December 2004.
[3] A.J. Prince, "Details and results of spill experiments of cryogenic liquids onto land and water", Joint HSE and UKAEA, SRD Report, HSE/SRD/PD058/WP4, 1983.
[4] P.K. Raj, Large LNG fire thermal radiation—modeling issues and hazard criteria revisited, Proc. Saf. Prog. 24 (3) (2005) 192–202.
[5] TNO, Method for the Calculation of the Physical Effects of the Escape of Dangerous Material (Liquids and Gases), Pt. 1, Bureau of Industrial Safety, The Hague, The Netherlands, 1977.

[6] J.L. Woodward, An integrated model for discharge rate, pool spread, and dispersion from punctured process vessels, J. Loss Prev. Process Ind. 3 (1990) 33–37.
[7] J. Cook, J.L. Woodward, A new unified model for jet, dense, passive, and buoyant dispersion including droplet evaporation and pool modeling, in: Intern. Conf. and Exhibition on Safety Health & Loss Prevention in the Oil, Chemical and Process Industries, AIChE co-sponsor, Singapore, February 15–19, 1993.
[8] J.L. Woodward, K. Krishna, A. Bagais, Validation and Extension of Pool Evaporation Model 17th Annual International Conference and Workshop of Risk, Reliability, and Security, AIChE, CCPS, Jacksonville, FL, October 8–11, 2002, pp. 169–188.
[9] J.L. Woodward, A.J. Pierorazio, SS3G-An Integrated Risk Analysis Program using Engineering Principles for Building Damage Mary K O'Connor 2001 Annual Symposium, College Station, TX, October 30–31, 2001.
[10] Baker Eng. and Risk Consultants, Inc., "SafeSite$_{3G}$™ Theory Manual" Version 1.04, April 28, 2005.
[11] D. Nedelka, J. Moorhouse, R.F. Tucker, The montoir 35 m diameter LNG pool fire experiments, in: Proceedings of the Ninth International Conference on LNG, Nice, France, Session III, Paper 3, 17–20 October, 1989.
[12] G.A. Mizner, J.A. Eyer, Radiation from liquefied gas fires on water, Combust. Sci. Technol. 35 (1983) 33–57.
[13] P.K. Raj, A.N. Moussa, K. Aravamudan, Experiments involving pool and vapor fires from spills of LNG on water, NTIS AD-A077073, USCG Report GD-D-55-79, Washington, DC 20590, 1979.
[14] D.S. Burgess, J.N. Murphy, M.G. Zabetakis, "Hazards of LNG spillage of natural gas on water", Report No. 7448, US Dept of Interior, Bur. of Mines, Pittsburgh, November 1970.
[15] D.S. Burgess, J. Biordi, J. Murphy, "Hazards of spillage of LNG into water", PMSRC Report No. 4177, US Dept. of Interior, Bureau of Mines, September 1972.
[16] E.M. Drake, A.A. Jeje, R.C. Reid, Transient boiling of liquefied cryogens on a water surface. I. Nitrogen, methane and ethane, Int. J. Heat Mass Transfer 18 (1975) 361.
[17] A.K. Dincer, E.M. Drake, R.C. Reid, Boiling of liquid nitrogen and methane on water. The effect of initial water temperature, Int. J. Heat Transfer 20 (1976) 177–180.
[18] R.C. Reid, K.A. Smith, Confined boiling rates of liquefied petroleum gas on water, EE-77-S-02-4558, MIT, May 1978b.
[19] H.R. Chang, R.C. Reid, J.A. Fay, Boiling and spreading of liquid nitrogen and liquid methane on water, Int. Comm. Heat Mass Transfer 10 (1983) 253.
[20] G.F. Felbauer, J.H. Heigl, W. McQueen, R.H. Whipp, W.G. May, Spills of LNG on water-vaporization and downwind drift of combustible mixtures, Report No. EE61E-72, Esso Res. and Development Lab., May 1972.
[21] G.J. Boyle, A. Kneebone, Laboratory investigations into the characteristics of LNG spills on water. Evaporation, spreading, and vapor dispersion, API Report 6732, Shell Res. Ltd., Thornton, England, March 1973.
[22] E.M. Drake, A.A. Jeje, R.C. Reid, Transient boiling of liquefied cryogens on a water surface. II. Light hydrocarbon mixtures, Int. J. Heat Mass Transfer 18 (1975) 1369;
H.R. Chang, R.C. Reid, Spreading boiling model for instantaneous spills of liquefied petroleum gas (LPG) on water, J. Hazard. Mater. 7 (1983) 19–35.
[23] R.P. Koopman, B.R. Bowman, D.L. Ermak, Data and calculations of dispersion on 5 m^3 LNG spill tests, Lawrence Livermore National Lab. Report UCRL 52876, October 1979.
[24] M.C. Paranouskas, C.D. Lind, P.K. Raj, J.M. Cece, Vapor cloud explosion study, in: Proceeding of the Fifth International Conference of Liquefied Natural Gas, vol. II, Paper 12, 1980.
[25] G.W. Colenbrander, J.S. Puttock, Dense gas dispersion behavior: experimental observations and model developments, in: IChemE Symposium Series No. 80, Series 33, Rugby, UK, F66-F75, 1983.
[26] R.C. Reid, K.A. Smith, Behavior of LPG on water, Hydrocarbon Process. (1978) 117–121;
P. Shaw, F. Brisco, Evaporation from spills of hazardous liquids on land and water, UKAEA Report SRD R100, May 1978.
[27] J.M. Chatris, J. Quintela, J. Folch, E. Planas, J. Arnaldos, J. Casal, Experimental study of burning rate in hydrocarbon pool fires, Combust. Flame 126 (2001) 1373–1383.
[28] W. Lehr, D. Simecek-Beatty, Comparison of hypothetical LNG and fuel oil fires on water, J. Hazard. Mater. 107 (2004) 3–9.
[29] R. Pitblado, LNG terminal operations hazard zones, in: AIChE Center for Chemical Process Safety (CCPS) 19th Annual International Conf. on Emergency Planning Preparedness Prevention Response, Orlando, FL, June 29–July 1, 2004, p. 115.
[30] R. Pitblado, J. Baik, G.J. Hughes, C. Ferro, S.J. Shaw, Consequences of liquefied natural gas marine incidents, Proc. Saf. Prog. 24 (2) (2005) 108–114.
[31] J. Fay, Model of spills and fires from LNG and oil tankers, J. Hazard. Mater. B96 (2003) 171–188.
[32] V.V. Klimenko, Film boiling on a horizontal plate—new correlation, Int. J. Heat Mass Transfer 24 (1981) 69–79.
[33] Y. Quiao, H.M. West, M.S. Mannan, D.W. Johnson, J.B. Cornwell, Assessment of the effects of release variables on the consequences on LNG spillage onto water using FERC model, J. Hazard. Mater. 130 (2006) 155–162.
[34] F.T. Dodge, J.T. Park, J.C. Buckingham, R.J. Maggott, Revision and experimental verification of the hazard assessment computer system models for spreading, movement, dissolution and dissipation of soluble chemicals spilled onto water, US Coast Guard Report CG-D-35-83, 1983.
[35] J. Fay, The spread of oil slicks on a calm sea, Fluid Mechanics Lab. Report, Dept. of Mechanical Eng., MIT, Cambridge, Mass, 1969.